

Efficient Dual ADMMs for Sparse Compressive Sensing MRI Reconstruction

Yanyun Ding^a, Peili Li^b, Yunhai Xiao^{1c}, Haibin Zhang^a

^a*College of Applied Science, Beijing University of Technology, Beijing 100124, China*

^b*School of Mathematics and Statistics, Wuhan University, Wuhan 430072, China*

^c*School of Mathematics and Statistics, Henan University, Kaifeng 475000, China*

Abstract

Magnetic Resonance Imaging (MRI) is a kind of medical imaging technology used for diagnostic imaging of diseases, but its image quality may be suffered by the long acquisition time. The compressive sensing (CS) based strategy may decrease the reconstruction time greatly, but it needs efficient reconstruction algorithms to produce high-quality and reliable images. This paper focuses on the algorithmic improvement for the sparse reconstruction of CS-MRI, especially considering a non-smooth convex minimization problem which is composed of the sum of a total variation regularization term and a ℓ_1 -norm term of the wavelet transformation. The partly motivation of targeting the dual problem is that the dual variables are involved in relatively low-dimensional subspace. Instead of solving the primal model as usual, we turn our attention to its associated dual model composed of three variable blocks and two separable non-smooth function blocks. However, the directly extended alternating direction method of multipliers (ADMM) must be avoided because it may be divergent, although it usually performs well numerically. In order to solve the problem, we employ a symmetric Gauss-Seidel (sGS) technique based ADMM. Compared with the directly extended ADMM, this method only needs one additional iteration, but its convergence can be guaranteed theoretically. Besides, we also propose a generalized variant of ADMM because this method has been illustrated to be efficient for solving semidefinite programming in the past few years. Finally, we do extensive experiments on MRI reconstruction using some simulated and real MRI images under different sampling patterns and ratios. The numerical results demonstrate

¹Corresponding author

that the proposed algorithms significantly achieve high reconstruction accuracies with fast computational speed.

Keywords: Magnetic resonance imaging; non-smooth convex minimization; compressive sensing; symmetric Gauss-Seidel iteration; alternating direction method of multipliers.

1. Introduction

Magnetic Resonance Imaging (MRI) has become an indispensable imaging tool for diagnosing and evaluating a host of conditions and diseases. The MRI data acquisition system can be characterized as follows:

$$b = \mathcal{F}u + \epsilon, \quad (1)$$

where u denotes the vectorized MR image formed by row/column concatenation of an image matrix, b is the collected k -space data, \mathcal{F} is the Fourier operator which maps the image space to the k -space, and ϵ is the system noise assumed to be normally distributed. The goal is to reconstruct u from the given collected k -space data b . However, this data acquisition process is quite time consuming due to physiological and hardware constraints.

The compressive sensing (CS) [3, 10] MRI is an effective approach allowing for data sampling much lower without significantly degrading the image quality. Let \mathcal{P} be an under-sampling mask on the k -space as shown in [12, 15, 25], and further let $K := \mathcal{P}\mathcal{F}$, i.e., $K : \mathbb{R}^d \rightarrow \mathbb{R}^p$ ($p \ll d$) is a partial Fourier transform matrix [5]. The undersampling process form of the sparse CS-MRI reconstruction can be mathematically modeled as

$$\min_{u \in \mathbb{R}^d} \{F(u) : Ku = b\},$$

where $F : \mathbb{R}^d \rightarrow \mathbb{R}$ is a sparse-promoting function, and $b \in \mathbb{R}^p$ represents the undersampled data. We should mention that F is a good sparse approximation under a certain transform, such as gradient operator [4] or wavelet transform[1]. The earlier works of

Email addresses: dingyanyunhenu@163.com (Yanyun Ding), lipeili@whu.edu.cn (Peili Li), yhxiao@henu.edu.cn (Yunhai Xiao), zhanghaibin@bjut.edu.cn (Haibin Zhang)

Lustig et al. [21] and He et al. [14] modeled the MRI reconstruction as a linear combination of wavelet sparsity and total variation (TV) regularization [30]. More precisely, denote $W \in \mathbb{R}^{q \times d}$ be a Haar wavelet transform matrix and $\Lambda := \text{diag}(\lambda_1, \lambda_2, \dots, \lambda_q)$ with $\lambda_i \geq 0$ be a diagonal matrix, the CS-MRI model using TV and wavelet is modeled as follows

$$\min_{u \in \mathbb{R}^d} \{\mu \|u\|_{\text{TV}} + \|\Lambda W u\|_1 : Ku = b\}, \quad (2)$$

where $\|\cdot\|_{\text{TV}}$ is a discretization of TV regularization, and $\mu > 0$ is a regularization parameter.

It is observed that both terms involved in the objective function of (2) are not differentiable, which causes main challenges for solving. Over the past decades, great efforts have been made to tackle this difficulty from different aspects. For examples, the nonlinear inverse scale space method of He et al. [14] has the capability to solve (2) approximately and has been demonstrated to be more straightforward and more efficient. The operator splitting method of Ma et al. [22] targets to an inclusion problem resulting from the first-order optimality condition of a related problem of (2). It is worthy of noting that both algorithms specifically solve a penalized variant of problem (2) rather than itself. The recent work of Li et al. [17] solves problem (2) directly based on the fact that the dual formulation of (2) is essentially a convex composite optimization problem with separable structures. Consequently, Li et al. [17] developed a two-step fixed-point proximity algorithm (2SFPPA) and demonstrated its numerical efficiency through a series of experiments. Besides, there are other reconstruction approaches that can yield high quality images without significantly increasing the computational cost, e.g., the methods in [2, 8] not only keep regularity of smooth part of images, but also preserve the edges in images; the method in [27] makes use of similarity in images to establish a general patch-based nonlocal operator to provide sparse representation of similar patches; the method in [24] uses the dependencies of the wavelet domain coefficients to accelerate MRI data acquisition.

Unlike almost all the methods mentioned above, in this paper, we focus on the dual problem of (2) which has favourable structures of three separable variables blocks and two separable non-smooth blocks. Nevertheless, we note that the directly extended alternating direction method of multipliers (ADMM) must be avoided because the type

of this method might diverge if the non-smooth blocks exceed two [6]. To resolve this dilemma, we employ the simple but very powerful symmetric Gauss-Seidel (sGS) technique [19, 18] which updates one of the variables merely twice, but it can guarantee convergence theoretically. The advantage of using the sGS technique is that it decomposes a large problem into several smaller pieces and then solves them correspondingly via their favorable structures, see e.g., [7, 9, 16, 32, 33]. As a product, we also apply the generalized ADMM of Xiao et al. [33] for further performance evaluations. We do numerical experiments on MRI reconstruction under different sampling patterns and ratios to demonstrate that the proposed algorithms significantly achieve medium reconstruction accuracies with fast computational speed. We have to stress, though, that the classic ADMM with unit step-length is actually the Douglas-Rachford splitting method to the sum of two maximal monotone operators resulting from the dual formulation, our another motivation of targeting to the dual problem is that the linear operator $KK^\top : \mathbb{R}^p \rightarrow \mathbb{R}^p$ is involved, instead of $K^\top K : \mathbb{R}^d \rightarrow \mathbb{R}^d$ when ADMMs are used to the primal problem (2) directly.

The remaining parts of this paper are organized as follows. In section 2, we summarize some basic definitions or concepts in convex analysis and imaging science, and review the recent developments of ADMMs for subsequent algorithm's construction. In section 3, we do some preparations for solving the model (2). In section 4, we state our motivation, and present a couple of sGS technique based ADMMs subsequently. In section 5, we test both presented algorithms and do performance comparisons by several numerical experiments. Finally, we conclude our paper with some remarks in section 6.

2. Preliminary results

In this section, we list some basic concepts in convex analysis, review a couple of semi-proximal ADMMs for separable convex optimization. We quickly recall some preliminary results in convex analysis of Rockafellar [28]. Let \mathcal{H} be a finite-dimensional real Euclidean space endowed with an inner product $\langle \cdot, \cdot \rangle$ and its induced norm $\| \cdot \|$ respectively. A subset $\mathcal{C} \subseteq \mathcal{H}$ is said to be convex if $(1 - \lambda)x + \lambda y \in \mathcal{C}$ whenever $x, y \in \mathcal{C}$, and $\lambda \in (0, 1)$. The relative interior of \mathcal{C} is denoted by $\text{ri}(\mathcal{C})$. If \mathcal{C} is a closed convex set in \mathcal{H} , for any $z \in \mathcal{H}$, let $\Pi_{\mathcal{C}}(z)$ denote the metric projection of z onto \mathcal{C} , which is the optimal solution

of the minimization problem $\min_y \{\|y - z\|^2 \mid y \in \mathcal{C}\}$. Given $x \in \mathfrak{X}$, the orthogonal projection onto the ℓ_∞ -norm ball $\Pi_{\mathcal{B}_\infty^{(r)}}(x)$ with radius $r > 0$ is expressed as

$$\Pi_{\mathcal{B}_\infty^{(r)}}(x) = \min\{r, \max\{x, -r\}\}. \quad (3)$$

Similarly, for ℓ_2 -norm, the projection can be given explicitly by

$$\Pi_{\mathcal{B}_2^{(r)}}(x) = \frac{x}{\|x\|_2} \min\{r, \|x\|_2\}.$$

Moreover, a subset $\mathcal{K} \subseteq \mathcal{H}$ is called a cone if it is closed under positive scalar multiplication, i.e., $\lambda x \in \mathcal{K}$ with $\lambda > 0$ if $x \in \mathcal{K}$. A cone \mathcal{K} is called a convex cone if it is convex.

Let $f : \mathcal{H} \rightarrow (-\infty, +\infty]$ be a closed proper convex function, we denote by $\text{dom}(f)$ the effective domain of f , namely, $\text{dom}(f) = \{x \mid f(x) < +\infty\}$. The subdifferential of f at point $x \in \mathcal{H}$ is the set defined by

$$\partial f(x) := \{y \in \mathcal{H} \mid f(z) \geq f(x) + \langle y, z - x \rangle, \forall z \in \mathcal{H}\}.$$

Obviously, $\partial f(x)$ is a closed convex set while it is not empty. The multi-valued operator $\partial f : x \rightrightarrows \partial f(x)$ is shown to be maximal monotone. Let f^* denote the convex conjugate of f , i.e.,

$$f^*(y) := \sup_x \{\langle y, x \rangle - f(x)\} = -\inf_x \{f(x) - \langle y, x \rangle \mid x \in \mathcal{H}\}.$$

For a nonempty closed convex set \mathcal{C} , the symbol $\delta_{\mathcal{C}}(x)$ represents the indicator function over \mathcal{C} such that $\delta_{\mathcal{C}}(x) = 0$ if $x \in \mathcal{C}$ and $+\infty$ otherwise. The conjugate of an indicator function $\delta_{\mathcal{C}}(x)$ is named support function defined by $\delta_{\mathcal{C}}^*(x) = \sup\{\langle x, y \rangle \mid y \in \mathcal{C}\}$, and the subdifferential of $\delta_{\mathcal{C}}(x)$ at x is the normal cone of \mathcal{C} , i.e., $\partial \delta_{\mathcal{C}}(x) = \mathcal{N}_{\mathcal{C}}(x)$. It is not hard to deduce that the Fenchel conjugate of $\|x\|_p$ is $\|x\|_p^* = \delta_{\mathcal{B}_q^{(1)}}(x)$ where $\mathcal{B}_q^{(1)} := \{x \mid \|x\|_q \leq 1\}$ and $1/p + 1/q = 1$.

The Moreau-Yosida regularization [29] of a closed proper convex function f at $x \in \mathcal{H}$ is defined as

$$\psi_f(x) := \min_{y \in \mathcal{H}} \{f(y) + \frac{1}{2}\|y - x\|^2\}. \quad (4)$$

For any $x \in \mathcal{H}$, problem (4) has an unique optimal solution, which is called the proximal point of x associated with f , i.e.,

$$\text{prox}_f(x) := \arg \min_{y \in \mathcal{H}} \{f(y) + \frac{1}{2}\|y - x\|^2\}.$$

In particular, the proximal point of x associated with an indicator function $\delta_{\mathcal{C}}(x)$ reduces to the metric projection of x onto \mathcal{C} , i.e.,

$$\text{prox}_{\delta_{\mathcal{C}}}(x) = \arg \min_{y \in \mathcal{H}} \{ \delta_{\mathcal{C}}(y) + \frac{1}{2} \|y - x\|^2 \} = \arg \min_{y \in \mathcal{C}} \{ \frac{1}{2} \|y - x\|^2 \} = \Pi_{\mathcal{C}}(x). \quad (5)$$

We now turn to briefly review the definition of the discrete form of TV regularization [4, 30]. To simplify, we consider a 2-dimensional grayscale image U with size $d_1 \times d_2$. The isotropic TV is defined by

$$\|U\|_{\text{TV}} = \sum_{i=1}^{d_1} \sum_{j=1}^{d_2} \|\nabla U\|, \quad (6)$$

where ∇ denotes the forward finite difference operator on the vertical and horizontal directions, i.e.,

$$(\nabla U)_{i,j} = ((\nabla U)_{i,j}^1, (\nabla U)_{i,j}^2)$$

with

$$(\nabla U)_{i,j}^1 = \begin{cases} U_{i+1,j} - U_{i,j}, & \text{if } i < d_1, \\ U_{i,1} - U_{i,j}, & \text{if } i = d_1, \end{cases} \quad \text{and} \quad (\nabla U)_{i,j}^2 = \begin{cases} U_{i,j+1} - U_{i,j}, & \text{if } j < d_2, \\ U_{1,j} - U_{i,j}, & \text{if } j = d_2, \end{cases}$$

for $i = 1, \dots, d_1$ and $j = 1, \dots, d_2$. We note that the ℓ_2 -norm in (6) can be replaced by the ℓ_1 -norm, in which case the resulting TV is an anisotropic discretization. We point out that, the isotropic TV is often preferred over any anisotropic ones, both types of discretizations lead to the so-called staircasing effects.

3. Dual formulation and optimality condition

In this section, we do some necessary preparations for subsequent algorithms' development. At the first place, we reformulate the TV regularization $\|\cdot\|_{\text{TV}}$ as a function composed with a linear mapping. We note that all the notations used here are the same as those in [17] for convenience. The matrix Kronecker product is denoted as \otimes , and a matrix B with size $2d \times d$ is defined as

$$B = \begin{bmatrix} I_{d_2} \otimes D_{d_1} \\ D_{d_2} \otimes I_{d_1} \end{bmatrix},$$

where I is an identity matrix with appropriate size, and D_r is a $r \times r$ difference matrix with the following form

$$D_r = \begin{bmatrix} 1 & & & & -1 \\ -1 & 1 & & & \\ & & \ddots & \ddots & \\ & & & -1 & 1 \end{bmatrix}.$$

Moreover, for any $y \in \mathbb{R}^{2d}$, we define a function $\psi : \mathbb{R}^{2d} \rightarrow \mathbb{R}$ as

$$\psi(y) = \sum_{i=1}^d \|[y_i, y_{d+i}]\top\|.$$

With these definitions, then the isotropic TV in (2) can be expressed as

$$\|u\|_{\text{TV}} = \psi(Bu). \quad (7)$$

Moreover, for any $y \in \mathbb{R}^q$, we define a convex function $\varphi : \mathbb{R}^q \rightarrow \mathbb{R}$ as $\|\Lambda y\|_1 = \varphi(y)$, which yields for $W \in \mathbb{R}^{q \times d}$ such that $Wu \in \mathbb{R}^q$ and

$$\varphi(Wu) = \|\Lambda Wu\|_1. \quad (8)$$

Substituting (7) and (8) into (2) and recalling the definition of indicator function, it shows that the problem (2) can be reformulated as

$$\min_{u \in \mathbb{R}^d} \{\mu\psi(Bu) + \varphi(Wu) + \delta_{\{b\}}(Ku)\}, \quad (9)$$

where $\delta_{\{b\}}(Ku)$ implies $\delta_{\{b\}}(Ku) = 0$ if $Ku = b$ and $+\infty$ otherwise. Furthermore, denote $Bu = z_1 \in \mathbb{R}^{2d}$, $Wu = z_2 \in \mathbb{R}^q$ and $Ku = z_3 \in \mathbb{R}^p$, then problem (9) can be rewritten equivalently as

$$\begin{aligned} \min_{u, z_1, z_2, z_3} \quad & \mu\psi(z_1) + \varphi(z_2) + \delta_{\{b\}}(z_3) \\ \text{s.t.} \quad & Bu = z_1, Wu = z_2, Ku = z_3. \end{aligned} \quad (10)$$

The Lagrangian function associated with problem (10) is given by

$$\begin{aligned} \mathcal{L}(u, z_1, z_2, z_3; x_1, x_2, x_3) = & \mu\psi(z_1) + \varphi(z_2) + \delta_{\{b\}}(z_3) \\ & + \langle Bu - z_1, x_1 \rangle + \langle Wu - z_2, x_2 \rangle + \langle Ku - z_3, x_3 \rangle, \end{aligned}$$

where $x_1 \in \mathbb{R}^{2d}$, $x_2 \in \mathbb{R}^q$ and $x_3 \in \mathbb{R}^p$ are multipliers associated with constrains. The Lagrangian dual function of (10) is to minimize $\mathcal{L}(u, z_1, z_2, z_3; x_1, x_2, x_3)$ over (u, z_1, z_2, z_3) ,

that is

$$\begin{aligned} D(x_1, x_2, x_3) &= \inf_{u, z_1, z_2, z_3} \mathcal{L}(u, z_1, z_2, z_3; x_1, x_2, x_3) \\ &= -(\mu\psi)^*(x_1) - \varphi^*(x_2) - \delta_{\{b\}}^*(x_3), \end{aligned}$$

by noting the definition of the conjugate function and the fact that $B^\top x_1 + W^\top x_2 + K^\top x_3 = 0$. The Lagrangian dual problem of the original (10) is to maximize this dual function $D(x_1, x_2, x_3)$, which can equivalently be written as the following minimization problem with three separate blocks of variables and a single linear equality constraint:

$$\begin{aligned} \min_{x_1, x_2, x_3} \quad & (\mu\psi)^*(x_1) + \varphi^*(x_2) + \delta_{\{b\}}^*(x_3) \\ \text{s.t.} \quad & B^\top x_1 + W^\top x_2 + K^\top x_3 = 0 \\ & x_1 \in \mathbb{R}^{2d}, \quad x_2 \in \mathbb{R}^q, \quad x_3 \in \mathbb{R}^p. \end{aligned} \tag{11}$$

From the properties of conjugate for norm functions reviewed previously, we know that $(\mu\psi)^*(x_1) = \delta_{\mathcal{B}_2^{(\mu)}}(x_1)$, where $\mathcal{B}_2^{(\mu)} = \{y \in \mathbb{R}^{2d} \mid \| [y_i, y_{d+i}]^\top \| \leq \mu, \quad i = 1, \dots, d\}$ and $\varphi^*(x_2) = \delta_{\mathcal{B}_\infty^{(\lambda)}}(x_2)$, where $\mathcal{B}_\infty^{(\lambda)} = \{y \in \mathbb{R}^q \mid |y_i| \leq \lambda_i, \quad i = 1, \dots, q\}$. Then problem (11) transforms into the following form

$$\begin{aligned} \min_{x_1, x_2, x_3} \quad & \delta_{\mathcal{B}_2^{(\mu)}}(x_1) + \delta_{\mathcal{B}_\infty^{(\lambda)}}(x_2) + \langle b, x_3 \rangle \\ \text{s.t.} \quad & B^\top x_1 + W^\top x_2 + K^\top x_3 = 0 \\ & x_1 \in \mathbb{R}^{2d}, \quad x_2 \in \mathbb{R}^q, \quad x_3 \in \mathbb{R}^p. \end{aligned} \tag{12}$$

The Lagrangian function associated to the dual problem (12) takes the following form

$$\mathcal{L}(x_1, x_2, x_3; u) = \delta_{\mathcal{B}_2^{(\mu)}}(x_1) + \delta_{\mathcal{B}_\infty^{(\lambda)}}(x_2) + \langle b, x_3 \rangle - \langle u, B^\top x_1 + W^\top x_2 + K^\top x_3 \rangle,$$

where $u \in \mathbb{R}^d$ is a multiplier. Suppose that $(\bar{x}_1, \bar{x}_2, \bar{x}_3)$ is the optimal solution of problem (12). Then there exists a Lagrangian multiplier \bar{u} such that the following KKT system holds,

$$\begin{cases} 0 \in \mathcal{N}_{\mathcal{B}_2^{(\mu)}}(\bar{x}_1) - B\bar{u}, \\ 0 \in \mathcal{N}_{\mathcal{B}_\infty^{(\lambda)}}(\bar{x}_2) - W\bar{u}, \\ 0 = b - K\bar{u}, \\ 0 = B^\top \bar{x}_1 + W^\top \bar{x}_2 + K^\top \bar{x}_3, \end{cases} \tag{13}$$

where $\mathcal{N}_{\mathcal{B}_2^{(\mu)}}(\bar{x}_1)$ (resp. $\mathcal{N}_{\mathcal{B}_\infty^{(\lambda)}}(\bar{x}_2)$) is the normal cone to $\mathcal{B}_2^{(\mu)}$ (resp. $\mathcal{B}_\infty^{(\lambda)}$) at $\bar{x}_1 \in \mathcal{B}_2^{(\mu)}$ (resp. $\bar{x}_2 \in \mathcal{B}_\infty^{(\lambda)}$).

The model (12) has separable structure in terms of both the objective function and the constraint, and thus, it falls into the framework of ADMM. The directly extended ADMM has been implemented and illustrated its practical performance by Li et al. [17]. Nevertheless, the convergence of the directly extended ADMM can not be theoretically guaranteed. To address this issue, Li et al. [17] characterized the solutions of (12) in terms of fixed-point of a proximity related operator and developed an algorithm named 2SFPPA which is demonstrated to be very efficient for a CS-MRI reconstruction problem.

4. Solving problem (12) by sGS technique based ADMM and generalized ADMM

We observe that the dual model (12) contains three blocks of variables and two blocks of non-smooth convex functions, and hence it can be solved by the methods of sGS technique based ADMM (abbr. sGS-ADMM) and generalized ADMM (abbr. sGS-ADMM.G) with convergence guaranteed.

4.1. Solving problem (12) by sGS-ADMM

In this section, we target to employ the sGS-ADMM to solve (12) and establish its convergence. The augmented Lagrangian function associated with the problem (12) is defined by

$$\begin{aligned} \mathcal{L}_\sigma(x_1, x_2, x_3; u) &= \delta_{\mathcal{B}_2^{(\mu)}}(x_1) + \delta_{\mathcal{B}_\infty^{(\lambda)}}(x_2) + \langle b, x_3 \rangle \\ &\quad - \langle u, B^\top x_1 + W^\top x_2 + K^\top x_3 \rangle + \frac{\sigma}{2} \|B^\top x_1 + W^\top x_2 + K^\top x_3\|^2, \end{aligned}$$

where $\sigma > 0$ is a penalty parameter and $u \in \mathbb{R}^d$ is a multiplier. It is well-known that, starting from (x_1^0, x_2^0, x_3^0) , the classic augmented Lagrangian method of multipliers solves

$$(x_1^{k+1}, x_2^{k+1}, x_3^{k+1}) = \arg \min_{x_1, x_2, x_3} \mathcal{L}_\sigma(x_1, x_2, x_3; u^k) \quad (14)$$

at the current iteration and updates the multiplier u^{k+1} subsequently. Solving (14) for x_1 , x_2 and x_3 simultaneously can be difficult, since it ignores the favorable separable structure emerging in the objective function and the constraints. Alternatively, one

may try to replace (14) by directly extended ADMM with the Gauss-Seidel order that $x_1 \rightarrow x_2 \rightarrow x_3 \rightarrow u$. However, the type of the approach may diverge in theory, although it often performs much better numerically. To deal with this challenge, we apply the intelligent sGS technique [18], which groups x_1 as one block and (x_2, x_3) as another, and takes the cycle order $x_1 \rightarrow x_3 \rightarrow x_2 \rightarrow x_3 \rightarrow u$ instead of the usual $x_1 \rightarrow x_2 \rightarrow x_3 \rightarrow u$. More precisely, with the given $(x_1^k, x_2^k, x_3^k; u^k)$, the new iteration $(x_1^{k+1}, x_2^{k+1}, x_3^{k+1}; u^{k+1})$ is generated via the iterative scheme:

$$\begin{cases} x_1^{k+1} = \arg \min_{x_1 \in \mathbb{R}^{2d}} \{ \mathcal{L}_\sigma(x_1, x_2^k, x_3^k; u^k) + \frac{\sigma}{2} \|x_1 - x_1^k\|_{\mathcal{S}_1}^2 \}, \\ x_3^{k+1/2} = \arg \min_{x_3 \in \mathbb{R}^p} \{ \mathcal{L}_\sigma(x_1^{k+1}, x_2^k, x_3; u^k) + \frac{\sigma}{2} \|x_3 - x_3^k\|_{\mathcal{S}_3}^2 \}, \\ x_2^{k+1} = \arg \min_{x_2 \in \mathbb{R}^q} \{ \mathcal{L}_\sigma(x_1^{k+1}, x_2, x_3^{k+1/2}; u^k) + \frac{\sigma}{2} \|x_2 - x_2^k\|_{\mathcal{S}_2}^2 \}, \\ x_3^{k+1} = \arg \min_{x_3 \in \mathbb{R}^p} \{ \mathcal{L}_\sigma(x_1^{k+1}, x_2^{k+1}, x_3; u^k) + \frac{\sigma}{2} \|x_3 - x_3^k\|_{\mathcal{S}_3}^2 \}, \\ u^{k+1} = u^k - \tau \sigma (B^\top x_1^{k+1} + W^\top x_2^{k+1} + K^\top x_3^{k+1}), \end{cases} \quad (15)$$

where $\mathcal{S}_1 = (\tau_1 I_{2d} - BB^\top)$, $\mathcal{S}_2 = (\tau_2 I_q - WW^\top)$ and $\mathcal{S}_3 = (\tau_3 I_p - KK^\top)$ are positive semi-definite linear operators with some appropriate choices of τ_1 , τ_2 and τ_3 . As can be seen from the framework that an extra preparation step to compute $x_3^{k+1/2}$ is performed before computing x_2^{k+1} . We will show in the next subsection that this extra step can be done at moderate cost, so that the iterative process can be performed cheaply.

We now show that the iterative manner $x_3^{k+1/2} \rightarrow x_2^{k+1} \rightarrow x_3^{k+1}$ can be grouped together as one block (x_2^{k+1}, x_3^{k+1}) with a specially designed semi-proximal term. The fact is directly followed from the well-known sGS decomposition theorem of Li et al. [19] which can be stated as follows.

Lemma 4.1. *For $k \geq 0$, the x_2 - and x_3 - subproblems in (15) can be summarized as the following compact form:*

$$(x_2^{k+1}, x_3^{k+1}) = \arg \min_{x_2, x_3} \left\{ \mathcal{L}_\sigma(x_1^{k+1}, x_2, x_3; u^k) + \frac{\sigma}{2} \left\| \begin{pmatrix} x_2 \\ x_3 \end{pmatrix} - \begin{pmatrix} x_2^k \\ x_3^k \end{pmatrix} \right\|_{\mathcal{G}}^2 \right\}, \quad (16)$$

where \mathcal{G} is self-adjoint positive semi-definite linear operator.

PROOF. Let

$$\mathcal{H} = \mathcal{D} + \mathcal{M} + \mathcal{M}^*,$$

where

$$\mathcal{M} = \begin{pmatrix} 0 & WK^\top \\ 0 & 0 \end{pmatrix}, \quad \mathcal{D} = \begin{pmatrix} WW^\top & 0 \\ 0 & KK^\top \end{pmatrix}, \quad \mathcal{M}^* = \begin{pmatrix} 0 & 0 \\ \mathcal{K}W^\top & 0 \end{pmatrix}.$$

Furthermore, denote

$$\mathcal{G}_1 = \mathcal{M}\mathcal{D}^{-1}\mathcal{M}^* = \begin{pmatrix} WK^\top(KK^\top)^{-1}KW^\top & 0 \\ 0 & 0 \end{pmatrix},$$

and

$$\mathcal{G}_2 = \begin{pmatrix} \mathcal{S}_2 & 0 \\ 0 & \mathcal{S}_3 \end{pmatrix} = \begin{pmatrix} \tau_2 I_q - WW^\top & 0 \\ 0 & \tau_3 I_p - KK^\top \end{pmatrix},$$

then the desired conclusion is followed from the sGS decomposition theorem in [19, Theorem 1] by setting $\mathcal{G} = \mathcal{G}_1 + \mathcal{G}_2$.

Based on the result, we can rewrite (15) equivalently as follows

$$\begin{cases} x_1^{k+1} = \arg \min_{x_1 \in \mathbb{R}^{2d}} \{ \mathcal{L}_\sigma(x_1, x_2^k, x_3^k; u^k) + \frac{\sigma}{2} \|x - x_1\|_{\mathcal{S}_1}^2 \}, \\ (x_2^{k+1}, x_3^{k+1}) = \arg \min_{x_2, x_3} \left\{ \mathcal{L}_\sigma(x_1^{k+1}, x_2, x_3; u^k) + \frac{\sigma}{2} \left\| \begin{pmatrix} x_2 \\ x_3 \end{pmatrix} - \begin{pmatrix} x_2^k \\ x_3^k \end{pmatrix} \right\|_{\mathcal{G}}^2 \right\}, \\ u^{k+1} = u^k - \tau \sigma (B^\top x_1^{k+1} + W^\top x_2^{k+1} + K^\top x_3^{k+1}), \end{cases} \quad (17)$$

which reduces to the two-block semi-proximal ADMM. This equivalence is very important because the convergence can be easily followed by using the known convergence result [11]. To conclude this subsection, we present the convergence result of sGS-ADMM for solving (12).

Theorem 4.1. ([11, Theorem B.1]) *Suppose that the sequence $(x_1^k, x_2^k, x_3^k; u^k)$ is generated by the iterative scheme (15) from an initial point $(x_1^0, x_2^0, x_3^0; u^0)$. If $\tau \in (0, (1 + \sqrt{5})/2)$ and \mathcal{S}_1 , \mathcal{S}_2 , and \mathcal{S}_3 are positive semi-definite linear operators, the sequence $\{(x_1^k, x_2^k, x_3^k)\}$ converges to an optimal solution of the dual problem (12) and $\{u^k\}$ converges to an optimal solution of the primal problem (2).*

Remark 4.1. *One issue yet remained to be addressed is to choose the positive semi-definite linear operators \mathcal{S}_1 , \mathcal{S}_2 and \mathcal{S}_3 . From the theory in numerical algebra, we know that this goal can be achieved by $\tau_1 \geq \rho(BB^\top)$, $\tau_2 \geq \rho(WW^\top)$ and $\tau_3 \geq \rho(KK^\top)$, respectively, where $\rho(\cdot)$ denotes the spectral radius of a matrix.*

4.2. Implement details

Observing that each step of the iterative scheme (15) involves solving a convex minimization problem, we now illustrate that a simple closed-form solution is permitted for each subproblem, which leads to the framework easy to implement. Firstly, we can get for every $k = 0, 1, \dots$ that

$$\begin{aligned} x_1^{k+1} &= \arg \min_{x_1 \in \mathbb{R}^{2d}} \left\{ \mathcal{L}_\sigma(x_1, x_2^k, x_3^k; u^k) + \frac{\sigma}{2} \|x_1 - x_1^k\|_{\mathcal{S}_1}^2 \right\} \\ &= \Pi_{\mathcal{B}_2^{(\mu)}} \left(x_1^k - \frac{1}{\tau_1} B(B^\top x_1^k + W^\top x_2^k + K^\top x_3^k - \frac{1}{\sigma} u^k) \right), \end{aligned}$$

where the last equality is from (5). Secondly, for every $k = 0, 1, \dots$, we have

$$\begin{aligned} x_3^{k+1/2} &= \arg \min_{x_3 \in \mathbb{R}^p} \left\{ \mathcal{L}_\sigma(x_1^{k+1}, x_2^{k+1}, x_3; u^k) + \frac{\sigma}{2} \|x_3 - x_3^k\|_{\mathcal{S}_3}^2 \right\} \\ &= x_3^k - \frac{1}{\tau_3} K(B^\top x_1^{k+1} + W^\top x_2^k + K^\top x_3^k - \frac{1}{\sigma} u^k) - \frac{1}{\tau_3 \sigma} b. \end{aligned}$$

We note that the linear operator KK^\top makes x_3 is located in a p -dimensional subspace rather than the d -dimensional subspace if the primal problem (2) is targeted. Thirdly, for every $k = 0, 1, \dots$, the solution x_2^{k+1} can be obtained by

$$\begin{aligned} x_2^{k+1} &= \arg \min_{x_2 \in \mathbb{R}^q} \left\{ \mathcal{L}_\sigma(x_1^{k+1}, x_2, x_3^{k+1/2}; u^k) + \frac{\sigma}{2} \|x_2 - x_2^k\|_{\mathcal{S}_2}^2 \right\} \\ &= \Pi_{\mathcal{B}_\infty^{(\lambda)}} \left(x_2^k - \frac{1}{\tau_2} W(B^\top x_1^{k+1} + W^\top x_2^k + K^\top x_3^{k+1/2} - \frac{1}{\sigma} u^k) \right). \end{aligned}$$

The derivation processes indicate that each subproblem enjoys analytic solution provided by properly choosing the semi-proximal terms with respect to \mathcal{S}_1 , \mathcal{S}_2 and \mathcal{S}_3 .

In summary, we are ready to state the full steps of the sGS-ADMM while it is used to solve the dual model problem (12) as follows:

4.3. Solving problem (12) by generalized ADMM

This subsection is devoted to applying the generalized ADMM of Xiao et al.[33] to solve problem (12). Again, we view variable x_1 as one group and view (x_2, x_3) as another, and use the sGS techniqueis with order $x_3 \rightarrow x_2 \rightarrow x_1$ in the second group. Then the generalize ADMM obeys the following form while it is used to solve the dual problem

Algorithm: sGS-ADMM

Step 0. Choose starting point $(x_1^0, x_2^0, x_3^0; u^0)$. Choose positive constants τ_i such that \mathcal{S}_i ($i = 1, 2, 3$) are positive semi-definite. Choose positive constants $\sigma > 0$ and $\tau \in (0, (1 + \sqrt{5})/2)$. For $k = 0, 1, \dots$, do the following operations iteratively.

Step 1. Given x_1^k, x_2^k, x_3^k , and u^k , compute

$$x_1^{k+1} = \Pi_{\mathcal{B}_2^{(\mu)}} \left(x_1^k - \frac{1}{\tau_1} B (B^\top x_1^k + W^\top x_2^k + K^\top x_3^k - \frac{1}{\sigma} u^k) \right).$$

Step 2. Given x_1^{k+1}, x_2^k, x_3^k , and u^k , compute

$$x_3^{k+1/2} = x_3^k - \frac{1}{\tau_3} K (B^\top x_1^{k+1} + W^\top x_2^k + K^\top x_3^k - \frac{1}{\sigma} u^k) - \frac{1}{\tau_3 \sigma} b.$$

Step 3. Given $x_1^{k+1}, x_2^k, x_3^{k+1/2}$, and u^k , compute

$$x_2^{k+1} = \Pi_{\mathcal{B}_\infty^{(\lambda)}} \left(x_2^k - \frac{1}{\tau_2} W (B^\top x_1^{k+1} + W^\top x_2^k + K^\top x_3^{k+1/2} - \frac{1}{\sigma} u^k) \right).$$

Step 4. Given $x_1^{k+1}, x_2^{k+1}, x_3^{k+1/2}$, and u^k , compute

$$x_3^{k+1} = x_3^k - \frac{1}{\tau_3} K \left(B^\top x_1^{k+1} + W^\top x_2^{k+1} + K^\top x_3^{k+1/2} - \frac{1}{\sigma} u^k \right) - \frac{1}{\tau_3 \sigma} b.$$

Step 5. Given $x_1^{k+1}, x_2^{k+1}, x_3^{k+1}$, and u^k , compute

$$u^{k+1} = u^k - \tau \sigma (B^\top x_1^{k+1} + W^\top x_2^{k+1} + K^\top x_3^{k+1}).$$

(12), that is

$$\left\{ \begin{array}{l} x_1^{k+1} = \arg \min_{x_1 \in \mathbb{R}^{2d}} \{ \mathcal{L}_\sigma(x_1, \tilde{x}_2^k, \tilde{x}_3^k; \tilde{u}^k) + \frac{\sigma}{2} \|x_1 - \tilde{x}_1^k\|_{\mathcal{S}_1}^2 \}, \\ u^{k+1} = \tilde{u}^k - \sigma(B^\top x_1^{k+1} + W^\top \tilde{x}_2^k + K^\top \tilde{x}_3^k), \\ x_3^{k+1/2} = \arg \min_{x_3 \in \mathbb{R}^p} \{ \mathcal{L}_\sigma(x_1^{k+1}, \tilde{x}_2^k, x_3; u^{k+1}) + \frac{\sigma}{2} \|x_3 - \tilde{x}_3^k\|_{\mathcal{S}_3}^2 \}, \\ x_2^{k+1} = \arg \min_{x_2 \in \mathbb{R}^q} \{ \mathcal{L}_\sigma(x_1^{k+1}, x_2, x_3^{k+1/2}; u^{k+1}) + \frac{\sigma}{2} \|x_2 - \tilde{x}_2^k\|_{\mathcal{S}_2}^2 \}, \\ x_3^{k+1} = \arg \min_{x_3 \in \mathbb{R}^p} \{ \mathcal{L}_\sigma(x_1^{k+1}, x_2^{k+1}, x_3; u^{k+1}) + \frac{\sigma}{2} \|x_3 - \tilde{x}_3^k\|_{\mathcal{S}_3}^2 \}, \\ \tilde{\omega}^{k+1} = \tilde{\omega}^k + \rho(\omega^{k+1} - \tilde{\omega}^k), \end{array} \right. \quad (18)$$

where $\omega = (x_1, x_2, x_3, u)$, $\rho \in (0, 2)$, and \mathcal{S}_1 , \mathcal{S}_2 and \mathcal{S}_3 are positive semi-definite linear operators defined before. We note that if $\rho = 0$ and $\mathcal{S}_i = 1$ for $i = 1, 2, 3$, the scheme (18) reduces to (15) with unite steplength $\tau = 1$. By mimicking the proof of Lemma 4.1, we can obtain that the sGS iteration with order $x_3 \rightarrow x_2 \rightarrow x_1$ can be viewed together with an additional semi-proximal term based on linear operator. Therefore, the global convergence of corresponding algorithm for (18) can be obtained from the [33, Theorem 5.1], which can be stated as follows without proof.

Theorem 4.2. (*[33, Theorem 5.1]*) *Suppose that the sequence $(x_1^k, x_2^k, x_3^k; u^k)$ is generated by the iterative scheme (18) from an initial point $(x_1^0, x_2^0, x_3^0; u^0)$. If $\rho \in (0, 2)$ and $\mathcal{S}_1, \mathcal{S}_2$, and \mathcal{S}_3 are positive semi-definite linear operators, the sequence $\{(x_1^k, x_2^k, x_3^k)\}$ converges to an optimal solution of the dual problem (12) and $\{u^k\}$ converges to an optimal solution of the primal problem (2).*

To end this subsection, we list the full steps of sGS-ADMM_G while it is used to solve the dual problem (12).

5. Numerical experiments

In this section, we construct a series of numerical experiments to evaluate the practical performance of sGS-ADMM and sGS-ADMM_G against the state-of-the-art algorithm 2SFPPA. All the experiments are performed with Microsoft Windows 10 and MATLAB R2018a, and run on a PC with an Intel Core i7 CPU at 1.80 GHz and 8 GB of memory.

Algorithm: sGS-ADMM_G

Step 0. Choose starting point $(x_1^0, x_2^0, x_3^0; u^0)$. Choose positive constants τ_i such that \mathcal{S}_i ($i = 1, 2, 3$) are positive semi-definite. Choose positive constants $\sigma > 0$ and $\rho \in (0, 2)$. For $k = 0, 1, \dots$, do the following operations iteratively.

Step 1. Given $\tilde{x}_1^k, \tilde{x}_2^k, \tilde{x}_3^k$, and \tilde{u}^k , compute

$$x_1^{k+1} = \Pi_{\mathcal{B}_2^{(\mu)}} \left(\tilde{x}_1^k - \frac{1}{\tau_1} B (B^\top \tilde{x}_1^k + W^\top \tilde{x}_2^k + K^\top \tilde{x}_3^k - \frac{1}{\sigma} \tilde{u}^k) \right).$$

Step 2. Given $x_1^{k+1}, \tilde{x}_2^k, \tilde{x}_3^k$, and \tilde{u}^k , compute

$$u^{k+1} = \tilde{u}^k - \sigma (B^\top x_1^{k+1} + W^\top \tilde{x}_2^k + K^\top \tilde{x}_3^k).$$

Step 3. Given $x_1^{k+1}, \tilde{x}_2^k, \tilde{x}_3^k$, and u^{k+1} , compute

$$x_3^{k+1/2} = \tilde{x}_3^k - \frac{1}{\tau_3} K \left(B^\top x_1^{k+1} + W^\top \tilde{x}_2^k + K^\top \tilde{x}_3^k - \frac{1}{\sigma} u^{k+1} \right) - \frac{1}{\tau_3 \sigma} b.$$

Step 4. Given $x_1^{k+1}, \tilde{x}_2^k, x_3^{k+1/2}$, and u^{k+1} , compute

$$x_2^{k+1} = \Pi_{\mathcal{B}_\infty^{(\lambda)}} \left(\tilde{x}_2^k - \frac{1}{\tau_2} W (B^\top x_1^{k+1} + W^\top \tilde{x}_2^k + K^\top x_3^{k+1/2} - \frac{1}{\sigma} u^{k+1}) \right).$$

Step 5. Given $x_1^{k+1}, x_2^{k+1}, \tilde{x}_3^k$, and u^k , compute

$$x_3^{k+1} = \tilde{x}_3^k - \frac{1}{\tau_3} K \left(B^\top x_1^{k+1} + W^\top x_2^{k+1} + K^\top \tilde{x}_3^k - \frac{1}{\sigma} u^{k+1} \right) - \frac{1}{\tau_3 \sigma} b.$$

Step 6. Given $x_1^{k+1}, x_2^{k+1}, x_3^{k+1}$, and u^{k+1} , compute

$$\tilde{\omega}^{k+1} = \tilde{\omega}^k + \rho (\omega^{k+1} - \tilde{\omega}^k).$$

5.1. General descriptions

First of all, some descriptions should be given for the following series of tests. We conduct experiments on some typical MRI data: a ‘‘Shepp-Logan’’ phantom, some brain images. We do the reconstruction from the retrospectively undersampled Fourier coefficients of these images. The k-space undersampling is simulated by using the following masks: Cartesian sampling with random phase encoding [21], 2D random sampling [21, 26, 27], pseudo radial sampling [31]. The Haar wavelet transform $W \in \mathbb{R}^{q \times d}$ is chosen to be non-decimated and thus we have that $q = 4d$. We set parameters in objective function be same as the reference [17]. Accordingly, we set the diagonal entries of the diagonal matrix Λ as follows

$$\lambda_i = \begin{cases} 0, & i \in \{1, 2, \dots, d\}, \\ \frac{1}{2}, & i \in \{d+1, d+2, \dots, q\}, \end{cases}$$

and take the regularization parameter in (2) as $\mu = 3$. For the 2SFPPA, we compile the code according to the Algorithm 1 in [17], and set the parameters $\alpha_1 = 1/8$ and $\alpha_2 = \alpha_3 = 0.9$, which have been illustrated to be able to achieve the best results in most cases for each dataset. For the other algorithms, we fix $\tau_1 = 8$, and $\tau_2 = \tau_3 = 10/9$. Besides, the steplength τ involved in sGS-ADMM is set to be the thumb value 1.618, and the relaxation factor in sGS-ADMM.G is set as $\rho = 1.4$.

Here, we use the peak signal-to-noise ratio (PSNR) in the unit of dB to measure the quality of the restored images, i.e.,

$$\text{PSNR} := 10 \log_{10} \frac{255\sqrt{d}}{\|\bar{u} - u\|} (\text{dB}).$$

Moreover, different from [20, 27], we adopt a couple of rigorous criteria in evaluating the validity of the involved algorithms. First, we use the relative ℓ_2 -norm error (RLNE) defined as

$$\text{RLNE} := \frac{\|\bar{u} - u\|}{\|u\|},$$

where \bar{u} is the ground truth image and u is the reconstructed image. Second, based on KKT system (13), we use the following KKT residuals criterion defined as

$$\text{RelErr} := \max\{\eta_P, \eta_D, \eta_1, \eta_2\},$$

where

$$\left\{ \begin{array}{l} \eta_P := \frac{\|Ku - b\|}{1 + \|b\|}, \\ \eta_D := \|B^\top x_1 + W^\top x_2 + K^\top x_3\|, \\ \eta_1 := \frac{\|x_1 - \Pi_{\mathcal{B}_2^{(\mu)}}(x_1 + Bu)\|}{1 + \|x_1\| + \|Bu\|}, \\ \eta_2 := \frac{\|x_2 - \Pi_{\mathcal{B}_\infty^{(\lambda)}}(x_2 + Wu)\|}{1 + \|x_2\| + \|Wu\|}. \end{array} \right.$$

In order to balance the primal and dual infeasibilities for accelerating the iteration of both presented algorithms, we use the variable penalty parameters strategies defined as follows. Moreover, 2SFPPA also use this updating technique for comparisons in a fair way. We initialize $\sigma_0 = 5e - 3$ (resp. β_0 in 2SFPPA) and update iteratively via the following form:

$$\sigma_{k+1} = \left\{ \begin{array}{ll} \min\{1.25\sigma_k, 10^{-2}\}, & \text{if } \eta_P/\eta_D \leq 1/5, \\ \max\{0.8\sigma_k, 10^{-5}\}, & \text{if } \eta_P/\eta_D \geq 5, \\ \sigma_k, & \text{otherwise.} \end{array} \right.$$

The iterative process of each algorithm is terminated if RelErr or RLNE is sufficiently small, or the maximum iteration number is achieved. We tried different starting points for each algorithm and found that all of them are insensitive towards starting points. Therefore, we initialize $(x_1^0, x_2^0, x_3^0, u^0)$ as zero in all experiments of the following.

5.2. Experiments on phantom data

In this subsection, we test the efficiency of each algorithm using a simple ‘‘Shepp-Logan’’ phantom image with size 256×256 as shown at leftmost plot in Figure 1. The sampling pattern is simulated by using the pseudo radial sampling mask with sampling rate 6.5% which is displayed at the second plot in Figure 1. In this test, we consider the noiseless case, i.e., $\epsilon = 0$ in (1).

Firstly, we compare the reconstruction qualities obtained by each algorithm within 100 iterations. The recovery images produced by 2SFPPA, sGS-ADMM and sGS-ADMM.G are listed from the third to the last plot in Figure 1, respectively. As can be observed from the last three images that, all the algorithms produced acceptable reconstructions within so few number of iterations. To be precise, 2SFPPA obtained an image with

RLNE = 7.21%, which is slightly larger than 2.38% and 2.17% derived by other two algorithms. To further visibly illustrate the superiority of the ADMMs, we draw the 10 times scaled difference images of (c-e) in Figure 1 to the true image (a). The compared heat images are listed in Figure 2, respectively. We observe that the reconstructed images of sGS-ADMM and sGS-ADMM.G exhibit obvious benefits compared with 2SFPPA.

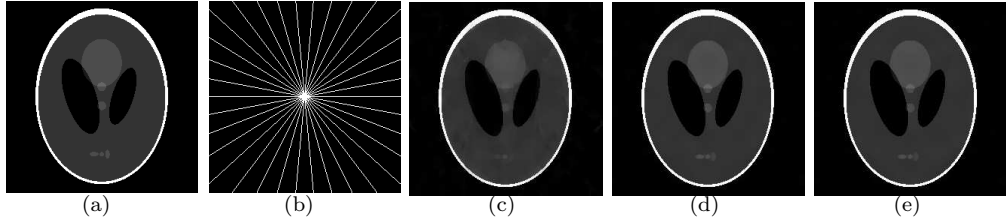


Figure 1: Reconstruction results using the phantom image: (a) the true image, (b) the pseudo radial sampling pattern of sampling rate 6.5%, (c)-(e) the reconstructed images by 2SFPPA, sGS-ADMM and sGS-ADMM.G with the RLNE errors are 7.21%, 2.38% and 2.17% within 100 iterations, respectively.

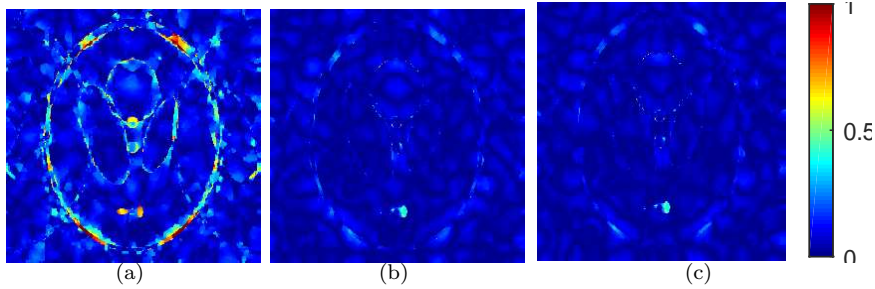


Figure 2: The $10\times$ scaled difference images of reconstructed images of 2SFPPA, sGS-ADMM and sGS-ADMM.G to the ground truth image.

Secondly, we determine each algorithm be successful if the criterion “ $RLNE \leq Tol$ ” is achieved. Then we investigate the numerical performance of each algorithm with different error tolerances Tol. In this test, we use the parameters values by default as the aforementioned except that the iterative process is forced to be terminated when maximum iterations 3000 is exceed without achieving convergence. We report the detailed results in Table 1 with respect to the numbers of iterations (‘Iter’), the PSNR values (‘PSNR’), and the computing time in seconds (‘CPU’) for “Shepp-Logan” phantom reconstruction.

In addition, the symbol “-” indicates that the corresponding algorithm cannot achieve the given accuracy within permissible number of iterations.

Table 1: Numerical comparisons results for “Shepp-Logan” phantom

| Algorithm | Tol = 10^{-2} | | | Tol = 10^{-3} | | | Tol = 10^{-4} | | |
|------------|-----------------|----------|------|-----------------|----------|-------|-----------------|----------|-------|
| | Iter | PSNR(dB) | CPU | Iter | PSNR(dB) | CPU | Iter | PSNR(dB) | CPU |
| 2SFPPA | 182 | 50.2 | 26.3 | 1804 | 60.2 | 299.8 | — | — | — |
| sGS-ADMM | 166 | 50.2 | 28.6 | 616 | 60.3 | 127.9 | 1754 | 70.2 | 291.3 |
| sGS-ADMM.G | 135 | 50.3 | 20.3 | 739 | 60.2 | 121.3 | 1951 | 70.2 | 290.9 |

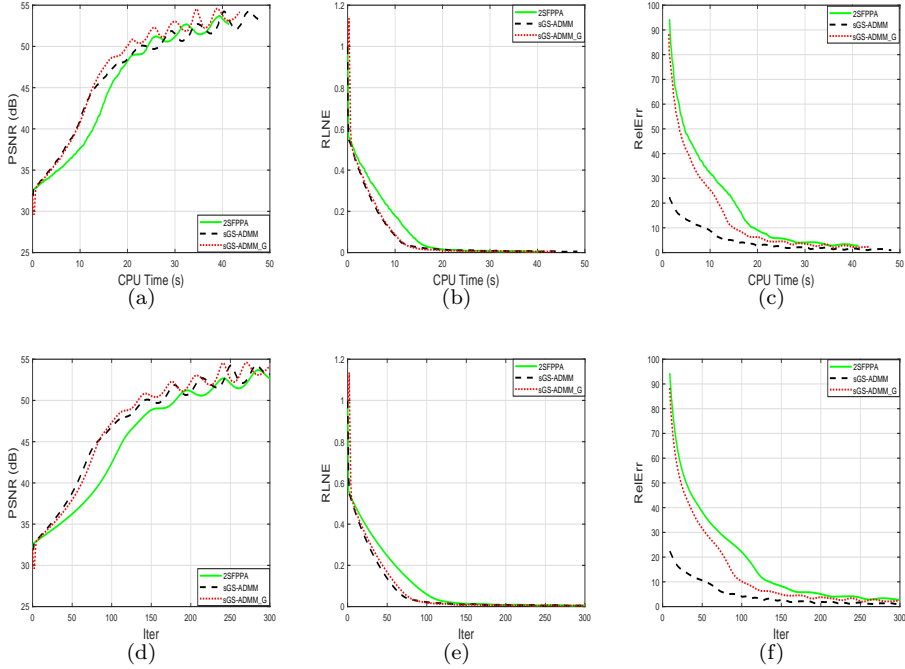


Figure 3: Reconstruction results using the phantom image. (a) PSNR versus computational time; (b) RLNE versus computational time; (c) RelErr versus computational time; (d) PSNR versus number of iterations; (e) RLNE versus number of iterations; (f) RelErr versus number of iterations.

We can observe from this table that almost all the tested algorithms can work successfully to produce the reconstructions except 2SFPPA failed to derive higher precision solutions. All the algorithms require more iterations and computing time with the improvement of accuracy, and the ADMM type methods apparently perform much better

than 2SFPPA. To more visually examine the algorithms' performance, we draw the curves of PSNR, RLNE and RelErr with respect to the iteration numbers and running time increase in Figure 3. It is worth mentioning that we abandoned the first 10 iterations in order to better highlight the trend of RelErr curve in the plots of righthand side. We find that the RelErr values are always higher than the RLNE values in the iteration process, so the stopping criteria can be chosen as $RLNE \leq Tol = 5e - 3$ or the maximum iteration number 300 is achieved. As can be seen from the two plots at the lefthand side of this figure, the curves derived by 2SFPPA are almost always at the bottom which indicate that 2SFPPA is the slowest to increase the PSNR values. The downward trend of RLNE and RelErr shows that all the algorithms are effective in the middle and the right side plots. Moreover, the sGS-ADMM and sGS-ADMM_G decrease faster than that from 2SFPPA in sense of RLNE and RelErr values. In summary, those simple tests preliminarily illustrate the efficiency of these employed algorithms in recovering phantom images.

5.3. Experiments on brain imaging data

In this subsection, we further investigate the validity of sGS-ADMM and sGS-ADMM_G. The experiments are conducted on a couple of T2-weighted brain images where the ground truth images with real and imaginary parts are shown in the first plots of Figures 4 and 5. The brain images to be tested are two slices acquired from a healthy volunteer at a 3T Siemens Trio Tim MRI scanners using the T2-weighted turbo spin echo sequence. The Figure 4 (a) is a 256×256 brain image ($TR/TE = 6100/99ms$, $FOV = 220 \times 220mm^2$, slice thickness = 3.0mm), and the Figure 5 (a) is another 512×512 brain image ($TR/TE = 5000/97ms$, $FOV = 230 \times 187mm^2$, slice thickness = 5.0mm). Again, the pseudo radial sampling scheme is used in these tests. The sampling rate of the foregoing image is chosen 18.11% as shown in Figure 4 (b), and 9.31% as shown in Figure 5 (b), respectively. As usual in MRI [13, 23], the i.i.d. complex Gaussian noise with standard deviation $\rho = 0.005$ is added to the k-space to verify the robustness of the algorithms. The last three plots (c-e) of Figures 4 and 5 represent the restoration results of algorithms 2SFPPA, sGS-ADMM and sGS-ADMM_G within 40 iterations for the two brain images, respectively.

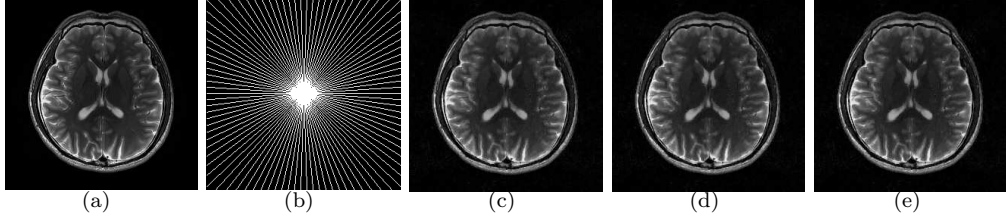


Figure 4: Reconstruction brain images 256×256 T2-brain images and using the pseudo radial sampling pattern of sampling rate 18.11%. (a) A full sampled brain image; (b) pseudo radial sampling mask; (c-e) reconstructed images by 2SFPPA, sGS-ADMM and sGS-ADMM_G, respectively.

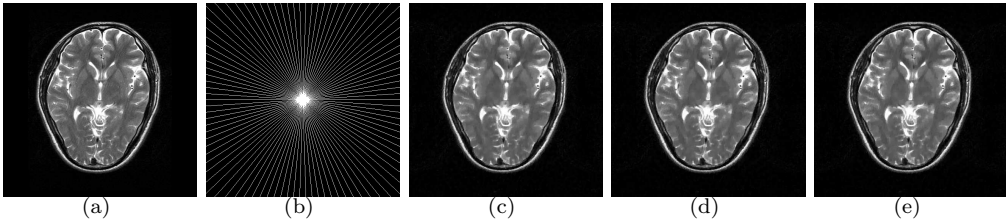


Figure 5: Reconstruction brain images 512×512 T2-brain images and using the pseudo radial sampling pattern of sampling rate 9.31%. (a) A full sampled brain image; (b) pseudo radial sampling mask; (c-e) Reconstructed images using 2SFPPA, sGS-ADMM and sGS-ADMM_G, respectively.

We can see that all the tested algorithms achieved the acceptable reconstruction results within so few iteration steps although it is hard to see the comparison results of the three algorithms clearly. To see the latent convergence behaviors of each algorithm, we draw some curves regarding PSNR, RLNE and RelErr of each algorithm for each tested image with respect to the time and iteration numbers. As before, we still abandon the previous 10 ill-conditioned iterations here when drawing the curves about RelErr. Details on each tested image can be found in Figures 6 and 7. As can be seen from these figures that, the results of sGS-ADMM_G fluctuated at the beginning, but it eventually been flat. From the PSNR curves, we can see that 2SFPPA has the fastest upward trend at the beginning, but sGS-ADMM caught up soon and kept the advantage to the end. This phenomenon is also happened similarly in the RLNE curves. For the curves derived by RelErr, we see that ADMM type methods decrease slightly faster than 2SFPPA as shown in the right plots. Based on the above explanations, we can conclude that the

ADMMs are really effective and practical in rebuilding real data of different sizes.

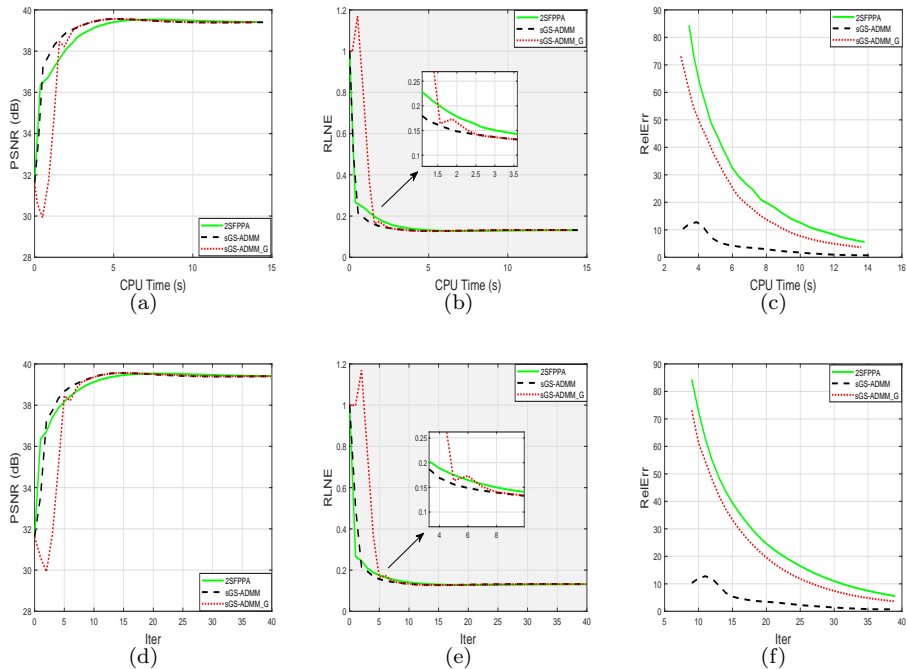


Figure 6: Reconstruction results of the brain image with size 256×256 . (a) PSNR versus computational time; (b) RLNE versus computational time; (c) RelErr versus computational time; (d) PSNR versus number of iterations; (e) RLNE versus number of iterations; (f) RelErr versus number of iterations.

5.4. Experiments using other undersampling patterns

It is well known that the undersampling patterns are very important to reduce reconstruction errors in MRI. In this part, we aim to show that capabilities of sGS-ADMM and sGS-ADMM_G are not limited to the pseudo radial sampling as tested previously, which also suitable for other undersampling patterns. In this subsection, we conduct experiments based on two typical patterns named the Cartesian sampling by random phase encoding of sampling rate 32.81% and 2D random sampling of sampling rate 30% listed at the left and the right of Figure 8, respectively. Besides, we test on six frequently used MR images in the literature with size 256×256 as shown in Figure 9. Moreover, the Gaussian noise as same as the aforementioned one is considered in these experiments. The

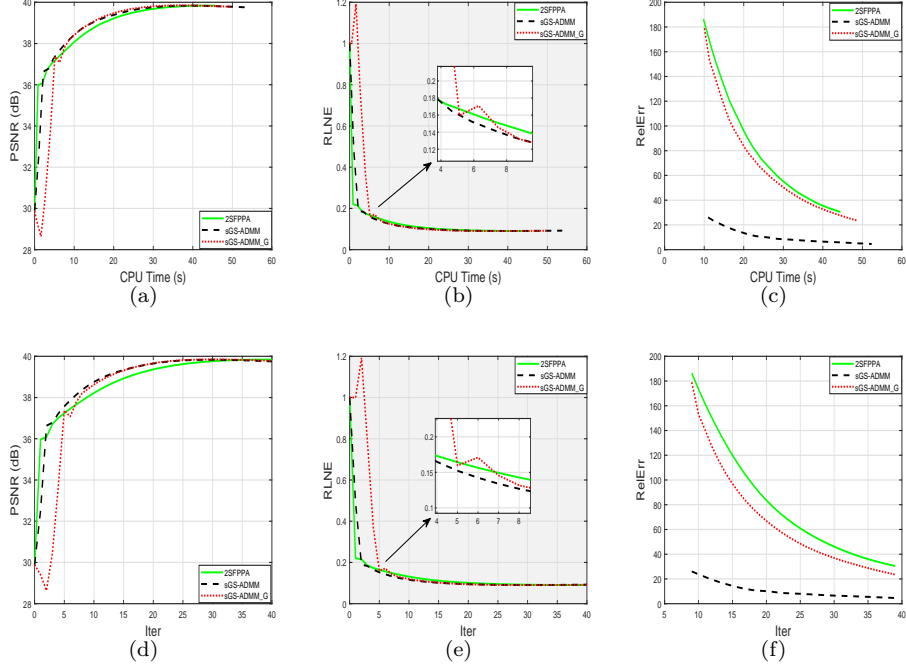


Figure 7: Reconstruction results of the brain image with size 512×512 . (a) PSNR versus computational time; (b) RLNE versus computational time; (c) RelErr versus computational time; (d) PSNR versus number of iterations; (e) RLNE versus number of iterations; (f) RelErr versus number of iterations.

numerical results derived by each algorithm with regarding to the final RLNE, RelErr, and PSNR values within 40 iterations are summarized in Table 2.

From this table, we observe that the three algorithms can effectively reconstruct these 9 kinds of MR images with different undersampling patterns. More precisely, the RLNE and RelErr values derived by sGS-ADMM and sGS-ADMM_G are always smaller than the one derived by 2SFPPA, which indicates that sGS-ADMM and sGS-ADMM_G always produce higher quality resolutions and in turn demonstrates that both presented algorithms are the winner in reconstructing MR images.

6. Conclusions

The extensive applications of compressed sensing MRI in clinical diagnosis has attracted much attention by many experts and scholars. It is generally believed in this

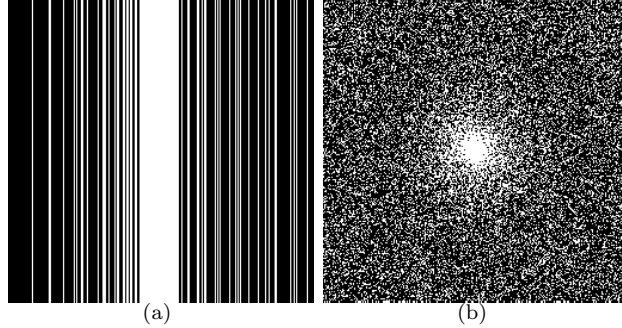


Figure 8: Sampling patterns to be used. (a) Cartesian sampling pattern with 32.81% data being sampled; (b) 2D random sampling pattern with 30% data being sampled.

Table 2: Numerical results of all the algorithms under other two different samplings

| Data | mask | 2SFPPA | | | sGS-ADMM | | | sGS-ADMM_G | | |
|-------------|-----------|--------|------|--------|----------|------|--------|------------|------|--------|
| | | RLNE | PSNR | RelErr | RLNE | PSNR | RelErr | RLNE | PSNR | RelErr |
| Figure 9(a) | Cartesian | 0.0442 | 46.8 | 23.7 | 0.0465 | 46.1 | 20.7 | 0.0411 | 47.0 | 18.7 |
| | 2D random | 0.0628 | 47.1 | 15.0 | 0.0677 | 46.6 | 13.7 | 0.0573 | 47.5 | 13.3 |
| Figure 9(b) | Cartesian | 0.2044 | 42.0 | 3.02 | 0.2012 | 42.1 | 2.42 | 0.2034 | 42.1 | 1.77 |
| | 2D random | 0.1685 | 45.2 | 3.06 | 0.1637 | 45.4 | 2.37 | 0.1662 | 45.3 | 1.82 |
| Figure 9(c) | Cartesian | 0.1668 | 44.1 | 2.54 | 0.1644 | 44.2 | 2.42 | 0.1660 | 44.1 | 1.76 |
| | 2D random | 0.1633 | 45.8 | 2.89 | 0.1606 | 45.9 | 2.51 | 0.1616 | 45.9 | 1.95 |
| Figure 9(d) | Cartesian | 0.1166 | 47.0 | 5.50 | 0.1168 | 46.7 | 3.68 | 0.1166 | 47.0 | 3.13 |
| | 2D random | 0.1164 | 48.1 | 3.98 | 0.1179 | 48.1 | 3.71 | 0.1162 | 48.2 | 3.12 |
| Figure 9(e) | Cartesian | 0.1220 | 44.1 | 4.45 | 0.1192 | 44.3 | 3.13 | 0.1208 | 44.2 | 2.68 |
| | 2D random | 0.1068 | 47.1 | 3.72 | 0.1044 | 47.2 | 3.28 | 0.1047 | 47.2 | 2.71 |
| Figure 9(f) | Cartesian | 0.1207 | 42.1 | 3.02 | 0.1180 | 42.3 | 2.66 | 0.1202 | 42.2 | 1.75 |
| | 2D random | 0.1400 | 43.4 | 3.70 | 0.1364 | 43.5 | 2.06 | 0.1388 | 43.4 | 1.93 |

communities that an advanced reconstruction algorithm plays a crucial rule in decreasing the acquisition time. In this paper, we took a dual approach to present a couple of efficient reconstruction algorithms for minimizing the sum of an ℓ_1 -norm of wavelet transformation term and TV regularization term. A series of numerical results on simulated phantom data and real brain imaging data with different undersampling patterns demonstrated the superior performance of sGS-ADMM and sGSADMM_G over the state-of-the-art solver 2SFPPA. The successes of both algorithms mainly lied in the successful using of the novel sGS technique which skillfully overcame the nonconvergent defect of traditional ADMM according to a very slightly computing cost. With the attractive

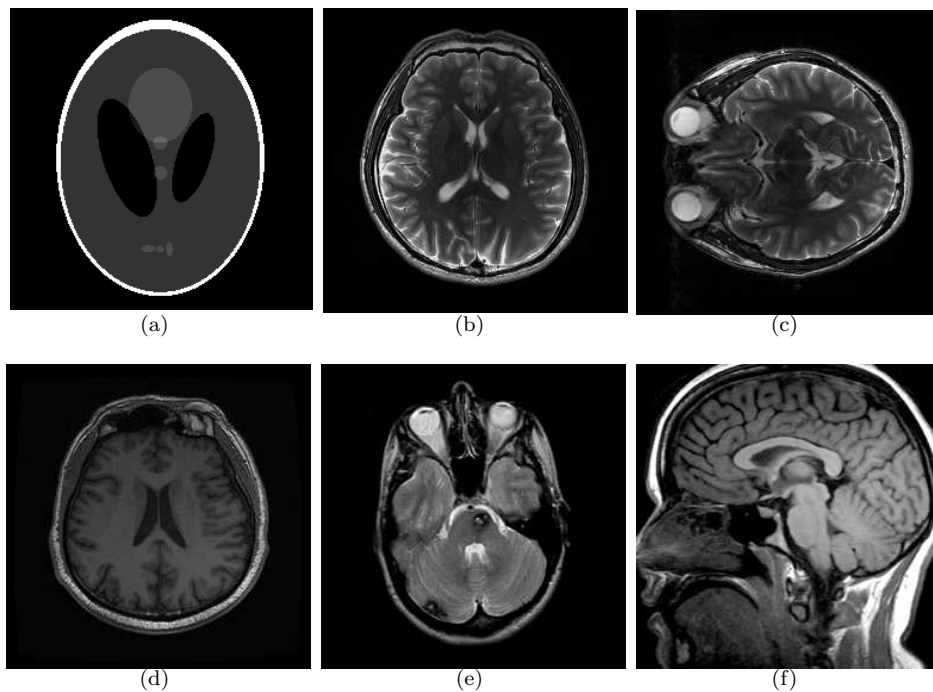


Figure 9: MR images to be tested with two different sampling patterns illustrated in Figure 8.

theoretical properties and the encouraging numerical performance, we believe that the sGS based ADMMs should have more potential applications in the field of CS in the near future.

Acknowledgements

The work of Y. Xiao is supported by the National Natural Science Foundation of China (Grant No. 11971149). The work of H. Zhang is supported by the National Natural Science Foundation of China (Grant No. 11771003).

References

References

- [1] J. Cai, R. H. Chan, L. Shen, Z. Shen, Convergence analysis of tight framelet approach for missing data recovery, *Advances in Computational Mathematics* 31 (2009) 87–113.

- [2] J. Cai, B. Dong, Z. Shen, Image restoration: A wavelet frame based model for piecewise smooth functions and beyond, *Applied and Computational Harmonic Analysis* 41 (2014) 94–138.
- [3] E. J. Candès, J. Romberg, T. Tao, Robust uncertainty principles: Exact signal reconstruction from highly incomplete frequency information, *IEEE Transactions on Information Theory* 52 (2006) 489–509.
- [4] T. F. Chan, S. Esedoglu, F. E. Park, A. M. Yip, Total variation image restoration: overview and recent developments, *Handbook of Mathematical Models in Computer Vision*, 2006.
- [5] T. F. Chan, J. Shen, H. Zhou, Total variation wavelet inpainting, *Journal of Mathematical Imaging and Vision* 25 (2006) 107–125.
- [6] C. Chen, B. He, Y. Ye, X. Yuan, The direct extension of admm for multi-block convex minimization problems is not necessarily convergent, *Mathematical Programming* 155 (2016) 57–79.
- [7] L. Chen, D. Sun, K. Toh, An efficient inexact symmetric gauss-seidel based majorized admm for high-dimensional convex composite conic programming, *Mathematical Programming* 161 (2017) 237–270.
- [8] B. Deka, S. Datta, S. Handique, Wavelet tree support detection for compressed sensing mri reconstruction, *IEEE Signal Processing Letters* 25 (2018) 730–734.
- [9] Y. Ding, Y. Xiao, Symmetric gauss-seidel technique-based alternating direction methods of multipliers for transform invariant low-rank textures problem, *Journal of Mathematical Imaging and Vision* 69 (2018) 1220–1230.
- [10] D. L. Donoho, Compressed sensing, *IEEE Transactions on Information Theory* 52 (2006) 1289–1306.
- [11] M. Fazel, T. K. Pong, D. Sun, P. Tseng, Hankel matrix rank minimization with applications to system identification and realization, *SIAM Journal on Matrix Analysis and Applications* 34 (2013) 946–977.
- [12] U. Gamper, P. Boesiger, S. Kozerke, Compressed sensing in dynamic mri, *Magnetic Resonance in Medicine: An Official Journal of the International Society for Magnetic Resonance in Medicine* 59 (2008) 365–373.
- [13] H. Gudbjartsson, S. Patz, The rician distribution of noisy mri data, *Magnetic Resonance in Medicine* 34 (1995) 910–914.
- [14] L. He, T. Chang, S. Osher, T. Fang, P. Speier, Mr image reconstruction from undersampled data by using the iterative refinement procedure, *PAMM: Proceedings in Applied Mathematics and Mechanics* 7 (2007) 1011207–1011208.
- [15] H. Jung, K. Sung, K. S. Nayak, E. Y. Kim, J. C. Ye, k-t focuss: a general compressed sensing framework for high resolution dynamic mri, *Magnetic Resonance in Medicine: An Official Journal of the International Society for Magnetic Resonance in Medicine* 61 (2009) 103–116.
- [16] P. Li, Y. Xiao, An efficient algorithm for sparse inverse covariance matrix estimation based on dual formulation, *Computational Statistics and Data Analysis* 128 (2018) 292–307.
- [17] Q. Li, Y. Xu, N. Zhang, Two-step fixed-point proximity algorithms for multi-block separable convex problems, *Journal of Scientific Computing* 70 (2017) 1204–1228.
- [18] X. Li, D. Sun, K. Toh, A schur complement based semi-proximal admm for convex quadratic conic

- programming and extensions, *Mathematical Programming* 155 (2016) 333–373.
- [19] X. Li, D. Sun, K. Toh, A block symmetric gauss-seidel decomposition theorem for convex composite quadratic programming and its applications, *Mathematical Programming* 175 (2019) 395–418.
- [20] Y. Liu, Z. Zhan, J. Cai, D. Guo, Z. Chen, X. Qu, Projected iterative soft-thresholding algorithm for tight frames in compressed sensing magnetic resonance imaging, *IEEE transactions on medical imaging* 35 (2016) 2130–2140.
- [21] M. Lustig, D. L. Donoho, J. M. Pauly, Sparse mri: The application of compressed sensing for rapid mr imaging, *Magnetic Resonance in Medicine: An Official Journal of the International Society for Magnetic Resonance in Medicine* 58 (2007) 1182–1195.
- [22] S. Ma, W. Yin, Y. Zhang, A. Chakraborty, An efficient algorithm for compressed mr imaging using total variation and wavelets, *IEEE Conference on Computer Vision and Pattern Recognition* (2008) 1–8.
- [23] E. R. Mcveigh, R. M. Henkelman, M. J. Bronskill, Noise and filtration in magnetic resonance imaging, *SIAM J. Numer. Anal.* 12 (1985) 586–591.
- [24] A. Mehmet, N. Seunghoon, H. Peng, M. Mehdi H., N. Long H., T. Vahid, M. Warren J., N. Reza, Compressed sensing with wavelet domain dependencies for coronary mri: a retrospective study., *IEEE Transactions on Medical Imaging* 30 (2011) 1090–1099.
- [25] H. Peng, M. Sabati, L. M. Lauzon, R. Frayne, Mr image reconstruction of sparsely sampled 3d k-space data by projection-onto-convex sets, *Magnetic resonance imaging* 24 (2006) 761–773.
- [26] X. Qu, D. Guo, B. Ning, Y. Hou, Y. Lin, S. Cai, Z. Chen, Undersampled mri reconstruction with patch-based directional wavelets, *Magnetic resonance imaging* 30 (2012) 964–977.
- [27] X. Qu, Y. Hou, F. Lam, D. Guo, J. Zhong, Z. Chen, Magnetic resonance image reconstruction from undersampled measurements using a patch-based nonlocal operator, *Medical image analysis* 18 (2014) 843–856.
- [28] R. T. Rockafellar, *Convex analysis*, Princeton university press, 1970.
- [29] R. T. Rockafellar, Monotone operators and the proximal point algorithm, *SIAM Journal on Control and Optimization* 14 (1976) 877–898.
- [30] L. Rudin, S. Osher, E. Fatemi, Nonlinear total variation based noise removal algorithms, *International symposium on physical design* 60 (1992) 259–268.
- [31] J. D. Trzasko, A. Manduca, Highly undersampled magnetic resonance image reconstruction via homotopic l_0 -minimization, *IEEE Transactions on Medical Imaging* 28 (2008) 106–121.
- [32] S. Wang, Y. Xiao, Z. Jin, An efficient algorithm for batch images alignment with adaptive rank-correction term, *Journal of Computational and Applied Mathematics* 346 (2019) 171–183.
- [33] Y. Xiao, L. Chen, D. Li, A generalized alternating direction method of multipliers with semi-proximal terms for convex composite conic programming, *Mathematical Programming Computation* 10 (2018) 533–555.